ADVANCED FUNCTIONAL MATERIALS
www.afm-journal.de

Capillary Condensation Mediated Fluidic Straining for Enhanced Bacterial Inactivation

Yuanyuan Zhao, Hubao A, Yuk Ha Cheung, Yintung Lam, Jiayue Tang, Han Li, Zhibing Yang, and John Haozhong Xin**

Biomaterials capable of continuously inactivating pathogens are essential for suppressing transmission of infectious diseases, such as epidemic cerebrospinal meningitis and pulmonary tuberculosis. Here, capillary condensation of air moisture within nano-confined spaces between superhydrophilic rigid nanorods is shown and target microbiology spontaneously stretch and inactivate aerosolized microorganisms. Specifically, the negative Gaussian curvature-shaped water condensate causes fluidic straining, comprising surface tension and Laplace pressure, strong enough to deform and eliminate the selected bacteria. Plate counting quantifies the sharply reduced contact-killing period for superhydrophilic and bare nanorods (6 vs 100 min for *E. coli*, 20 vs 120 min for *S. aureus*) under relative humidity of 70%. Theoretical calculations and experimental studies indicate increased mechanical straining and mechano-bactericidal by improving air moisture content. To further illustrate utility, long-term antibacterial medical masks are fabricated by integrating such nanorods onto commercial fabrics. Collectively, these findings highlight the immense potential of capillary condensation-induced fluidic straining as an eco-friendly, broad-spectrum, and highly efficient antibacterial strategy.

1. Introduction

Bacterial colonization can lead to infections, particularly in healthcare settings where medical devices are utilized.[1] To address this issue, strategies such as effective sterilization protocols and the development of antimicrobial materials and coatings for medical devices have been employed. A promising alternative is the use of mechano-bactericidal surfaces.[2–5] These surfaces are engineered to mechanically destroy bacteria by employing distinct micro or nano scale textures or patterns. Such a design directly harms bacterial cells when they come into contact, causing them to die. The primary benefit of these mechano-bactericidal surfaces is that they physically eliminate bacteria, bypassing the need for chemicals that might lead to antimicrobial resistance. This suggests that mechano-bactericidal surfaces offer a hopeful solution in the fight against bacterial growth and infections.

Capillary condensation occurs when water vapor condensates into confined geometries, such as soil particles and sugar powders, at a partial pressure (P) below the saturation vapor pressure (P_0), as described within Kelvin equation:[6–8]

$$\ln \frac{P}{P_0} = -\frac{2\gamma V_m \cos\theta}{r_1 RT} \tag{1}$$

where r_1 is the meniscus curvature radius of the condensed water; γ is the surface tension; V_m is molar volume of the condensate; θ is the contact angle of the water against the solid wall. Generally, capillary condensation will raise saddle-shaped bulk liquids that dynamically bridge wettable surfaces and cause strong attraction

Y. Zhao, Y. H. Cheung, Y. Lam, H. Li, J. H. Xin
School of Fashion and Textiles
The Hong Kong Polytechnic University
Hong Kong 999077, China
E-mail: tcxinjh@polyu.edu.hk

Y. Zhao, Y. H. Cheung, J. H. Xin
Shenzhen Research Institute
The Hong Kong Polytechnic University
Shenzhen 518057, China

H. A, Z. Yang
State Key Laboratory of Water Resources Engineering and Management
Wuhan University
Wuhan 430072, China
E-mail: zbyang@whu.edu.cn

H. A, Z. Yang
Key Laboratory of Rock Mechanics in Hydraulic Structural Engineering of the Ministry of Education
Wuhan University
Wuhan 430072, China

J. Tang
Sustainable Energy and Environment Thrust, Function Hub
Hong Kong University of Science and Technology (Guangzhou)
Guangzhou 511453, China

The ORCID identification number(s) for the author(s) of this article can be found under https://doi.org/10.1002/adfm.202314581

DOI: 10.1002/adfm.202314581

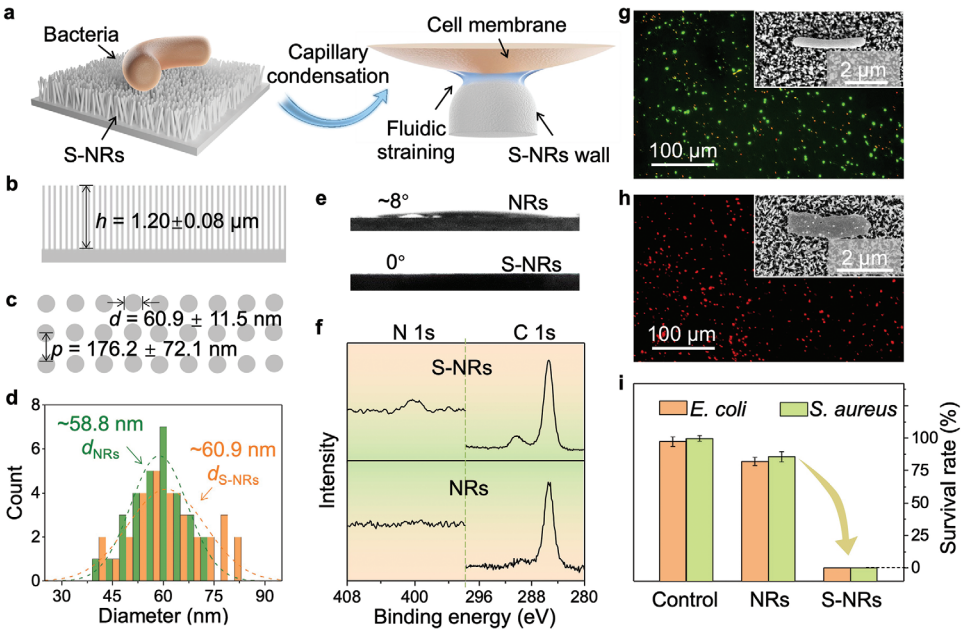

Figure 1. S-NRs for killing aerosolized bacteria. a) Conceptual design of capillary condensation mediated fluidic straining for enhanced biological aerosol disinfection. Spontaneous condensation of air moisture below saturation vapor pressure between the cell membrane and S-NRs wall will cause saddle-shaped liquids. The liquid meniscus will induce capillary straining, comprising surface tension and Laplace pressure. b,c) Schematic of S-NRs parameters. d,e) Diameter distribution and water contact angle images of NRs and S-NRs. f) High-resolution XPS of C 1s and N 1s peaks of NRs and S-NRs. Representative fluorescent microscope imaging of dead (red) and live (green) *E. coli* after deposition on NRs g) and S-NRs h). Insets are SEM images of single *E. coli*. i) *E. coli* and *S. aureus* survival rates on control, NRs, and S-NRs, showing the significantly improved bacteria-killing behaviors of S-NRs. The error bars represent standard deviations and $n = 5$ for each data point.

of bridged solids depending on air relative humidity (RH) and surface wettability.[9–20] In this work, we show that capillary condensation induced attraction between superhydrophilic nanostructures and the microorganisms causes substantial mechanical strain and deformation to significantly enhance mechano-bactericidal activity[2,21–25] (**Figure 1a**). Specifically, we find that the survival rates of representative aerosolized bacteria, *Staphylococcus aureus (S. aureus)* and *Escherichia coli (E. coli)*, deposited on our superhydrophilic nanorods (S-NRs) are significantly reduced in strong contrast with their unmodified NRs counterparts[26–29] (e.g., 40.8% vs 0% under RH of ≈30%). We reason that controlled formation of capillary straining within mechano-bactericidal systems offers an environmental-friendly routine for development of antibacterial strategies.

2. S-NRs for Improved Bacteria Killing

Zinc oxide (ZnO) demonstrates exceptional biocompatibility, safety, and enduring efficacy, rendering it apt for an array of biomedical applications.[30–32] ZnO nanorods demonstrate strong antibacterial characteristics, operating through various mechanisms like producing reactive oxygen species (ROS) when exposed to light, emitting Zn^{2+} ions, and physically harming bacterial cell membranes.[33] We have synthesized ZnO nanorods (NRs) using established hydrothermal methods, using them as a benchmark to evaluate the efficacy of our approach in enhancing bacterial inactivation.[34] To trigger capillary condensation between NRs tips and bacteria cell membrane,[2,21,35,36] we grafted highly hydrophilic polyvinylpyrrolidone (PVP) to the NRs and obtained S-NRs (Figure S1a,b, Supporting Information). We selected PVP also because of its nontoxicity, chemical stability, and easy immobilization onto solid surfaces.[37–39]

S-NRs have a height $h \approx 1.2$ μm and center-to-center spacing $p \approx 176$ nm (Figure 1b,c), with improved diameter $d_{S\text{-}NRs}$ ≈60.9 from 58.8 nm of NRs (Figure 1d), as determined by Scanning Electron Microscope (SEM) imaging (Figure S1c–f, Supporting Information). The observed diameters align closely with prior research, facilitating a direct comparison of antibacterial performance.[21,24,40,41] We found that contact angles of S-NRs were reduced to 0°, from Figure 1e, in strong contrast with NRs (≈8°). Subsequently, we evaluated the surface chemistry employing X-ray photoelectron spectroscopy (XPS, Figure 1f; Figure S2a, Supporting Information).[26,42] In detail, the peak at 399.8 eV is attributed to N 1s from pyrrole rings. The C 1s peaks of the PVP-modified NRs indicate two carbon components which are aliphatic carbon (284.8 eV) and amide (288.4 eV). We conducted Fourier-transform infrared spectroscopy (FTIR) to further analyze the NRs and S-NRs (Figure S2b,c, Supporting Information).[26,43,44] The absorption peak at 576 cm^{-1}, observed in both NRs and S-NRs, corresponds to the metal-oxygen (ZnO stretching vibrations) vibration mode. Our analysis also highlighted that the IR spectrum of S-NRs features a C=O stretching vibration peak at 1658 cm^{-1}, attributable to the amide group of PVP. Additionally, the S-NRs display stretching band peaks for $-CH_3$ at 2961 cm^{-1} and $-CH_2-$ at 2923 cm^{-1}. The NR contains hydroxyl groups and water molecules, either chemisorbed or physisorbed, evidenced by a broad absorption band ≈3440 cm^{-1}. This band is more pronounced in the S-NRs, reflecting their

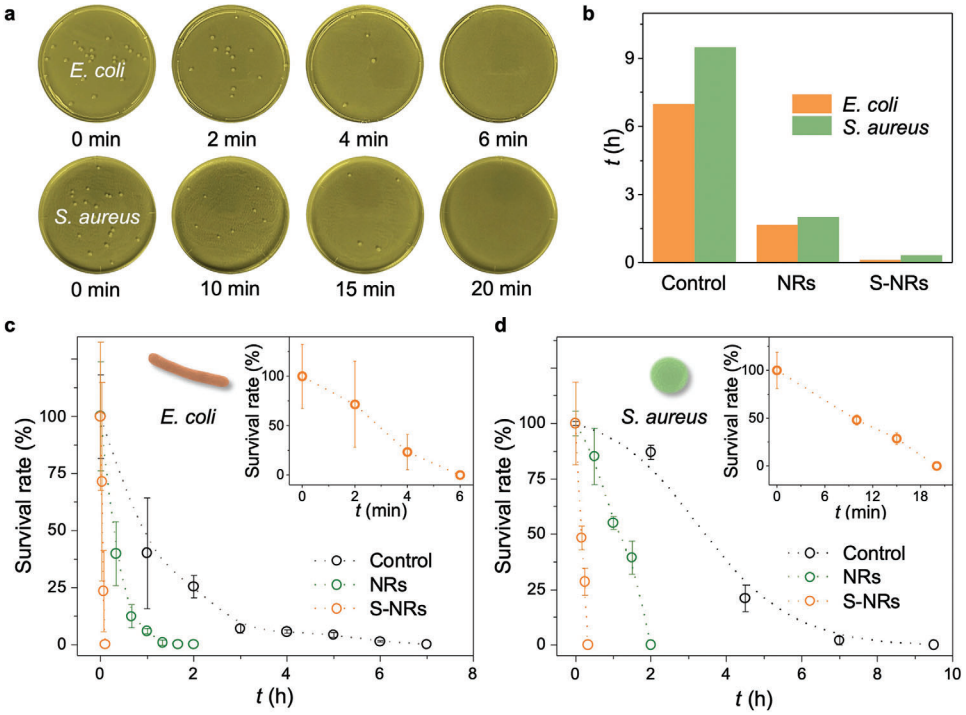

Figure 2. Detailed antibacterial performance of S-NRs. a) Optical images of representative agar plates of transferred airborne *E. coli* and *S. aureus* after exposure to S-NRs. b) Time required for killing all airborne bacteria deposited on the control, NRs, and S-NRs. c,d) Time-dependent *E. coli* and *S. aureus* survival rate on the above surfaces, showing the excellent antimicrobial property of S-NRs. The error bars represent standard deviations and $n = 5$ for each data point.

superior water absorption capabilities. Finally, energy dispersive X-ray (EDX) mapping of NRs and S-NRs confirmed the different element content of carbon and nitrogen (Figure S3, Supporting Information). The above-mentioned results indicated successful fabrication of S-NRs.

Subsequently, we investigated the antimicrobial activities of the S-NRs to bacteria–containing aerosols with Gram-negative *E. coli* and Gram-positive *S. aureus*, under RH of 70%, by observing the morphological changes of bacteria after contacting with the surfaces. All the antibacterial tests were conducted without light to focus on mechanical mechanism and to exclude the effect of reactive oxygen species. To study the bacteria-killing mechanism and behaviors, we chose bare glass (control), NRs, and S-NRs. We note that the ultrasound device effectively removes bacteria deposited on bare or modified glass without compromising their survival, as evidenced in Figure S4 (Supporting Information). By directly introducing bacterial suspensions (10^7 CFU mL^{-1}) in a consistent volume (10 µL) to all samples, we ensured an equal amount of bacteria was added. Post-ultrasound rinsing, all fluorescence vanished, suggesting the total removal of bacteria from the samples. To underscore that the ultrasound does not harm bacterial viability, we subjected both *S. aureus* and *E. coli* suspensions to the ultrasound. Observations reveal that the quantity of surviving bacteria remains consistent, regardless of ultrasound exposure, as seen in Figure S5 (Supporting Information).

In the antibacterial assays, the bacteria interfacing with the three surfaces were rinsed and stained utilizing a cell-nonpermeant red dye, namely propidium iodide (PI), which exclusively permeates cells possessing compromised membranes. Subsequently, they were counterstained employing a cell-permeant green dye (SYTO 9), capable of staining the nucleic acids in living cells. As demonstrated in Figure S6 (Supporting Information) and Figure 1g, many live *E. coli* (green) were found, with several dead ones, after contacting the control and NRs, showing that NRs possesses certain antimicrobial activity. In contrast, upon contact with the S-NRs, a substantial reduction in observed green fluorescence signals was detected, indicating the disruption or lysis of all bacterial cells (Figure 1h). This observation was further corroborated by the accompanying SEM figures. *E. coli* cells contacting the control and NRs maintained smooth surfaces and intact cell membranes, whereas cell membrane deformation and collapse were observed on cell exposed to S-NRs. Similarly, S-NRs surface shows excellent bacteria-killing property with *S. aureus* (Figure S7, Supporting Information). By evaluating survival rate from live/dead bacterial viability assay, we conclude that S-NRs show extraordinary antimicrobial activity (Figure 1i) in comparation with the control and NRs.

3. Detailed Antibacterial Performance of S-NRs

To further assess the antibacterial activity of S-NRs, we conducted the contact-killing assay at a series of contacting time under RH of 70% and challenged the ability via agar plate counting. The time-dependent representative bacteria colonies agar plates of the control, NRs, and S-NRs are shown in **Figures** 2a,b, and S8 and S9 (Supporting Information). The death of all the *E. coli* and *S. aureus* on the control took 7 and 9.5 h, respectively, while the NRs reduced the time to 1.7 and 2 h, respectively. Remarkably,

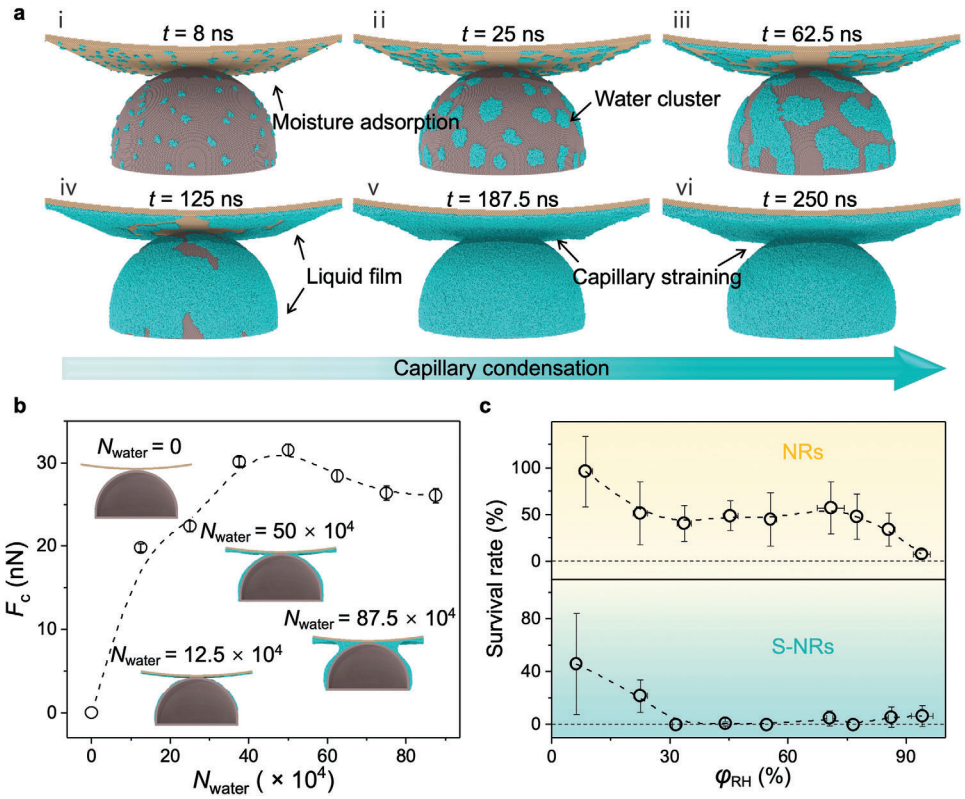

Figure 3. Capillary straining between bacteria and S-NRs. a) Simulated process of capillary straining between S-NR and bacteria. For clarity, vapor molecules are not plotted. b) Relationship between capillary straining force F_c and the number of water molecules N_{water} present in the simulation system. c) Dependence of bacterial survival rate on varying levels of RH (φ_{RH}). The error bars represent standard deviations and $n = 5$ for each data point.

S-NRs could disinfect airborne *E. coli* and *S. aureus* within 6 and 20 min, showing much higher antimicrobial potential. The cell wall of *S. aureus* has a thick peptidoglycan layer, which is a polymer composed of sugars and amino acids that form a mesh-like structure surrounding the cell. This layer provides rigidity and strength to the cell wall. Some Gram-positive bacteria, including *S. aureus*, also have teichoic acids, which are negatively charged polymers that contribute to the mechanical properties of the cell wall. In contrast, *E. coli* has a thinner peptidoglycan layer compared to *S. aureus*. The variation in the thickness of their peptidoglycan layers and the presence of an outer membrane causes the mechanical differences between the cell membranes of *S. aureus* and *E. coli*, which may cause the slight difference in contact-killing time.

We then calculated the survival rate of *E. coli* and *S. aureus* on three kinds of surfaces for various contacting time (Figure 2c,d). The above results exhibit the significantly improved bactericidal activity of S-NRs. After establishing the pronounced antibacterial capabilities of S-NRs, it was equally vital to discern the specific contribution of PVP in this mechanism. Understanding the crucial need to clarify PVP's role, we prepared a PVP@glass sample by incorporating PVP onto the bare glass. The differences in carbon and nitrogen elemental mapping, as illustrated in Figure S10a,b (Supporting Information) verify the successful preparation of PVP@glass. Furthermore, grafting PVP onto the glass resulted in a decrease in the water contact angle from 31° to 19°, as shown in Figure S10c (Supporting Information). When we compared its antibacterial properties with the unmodified bare glass, the outcomes were strikingly similar, as depicted in Figure S10d (Supporting Information). This similarity effectively dispels the notion that the observed enhanced antibacterial effect is solely due to the presence of PVP.

4. Working Mechanism of Capillary Straining of S-NRs

Molecular Dynamics (MD) simulations were performed to provide a comprehensive account of the condensation formation process between a S-NR and bacteria. The growth of condensation in a typical situation is illustrated by six representative time-lapse snapshots from the simulation system, as depicted in **Figure 3**a. i) Initially, vapor molecules adsorb onto the surfaces of both the S-NR and bacteria, aggregating into random clusters through molecular interactions, consisting of several or tens of water molecules (Figure 3a). ii) These clusters subsequently expand into droplets by adsorbing more vapor molecules, intriguingly taking on a film-like appearance due to the strong hydrophilicity of the S-NR and bacteria. iii,iv) As the condensation progresses, the water droplets continue to grow and coalesce into larger patches, eventually covering both the S-NR and bacterial surfaces with a liquid film. v,vi) Our simulation results also indicate that the majority of vapor molecules adsorb onto other

regions of the S-NR and bacterial surfaces before reaching the contact region, which accounts for the lack of an apparent liquid bridge in the early simulation stages. The size of the meniscus increases rapidly after the liquid film on the S-NR surface merges with that on the bacterial surface. In the subsequent simulation stages, both the liquid film thickness and the meniscus size increase due to the incorporation of additional vapor molecules.

The influence of humidity condition on the capillary straining between S-NRs and bacteria was quantified via the simulations at different RH levels represented by the number of water molecules within the simulation domain. Once the simulation system achieves equilibrium, we obtain the straining force exerted on the bacteria. As depicted in Figures 3b and S11 (Supporting Information), the straining force is strongly dependent on the number of water molecules in the simulation domain, that is, the *Fc* depends on the RH. Specifically, the force undergoes a sharp increase when the number of water molecules varies from 0 to 500 000, followed by a slight decline in more humid environments, which aligns with existing experimental observations.[45,46]

The dependence of the straining force on RH is closely related to the formation and size of the liquid condensates.[47] In low-humidity environments, the majority of vapor molecules adsorb onto the surfaces of the S-NR and bacteria, forming small clusters that may expand into larger droplets or films. However, no apparent capillary condensation forms in such scenarios, resulting in a minimal capillary straining force (as exemplified by the case with 125 000 water molecules). As RH increases, a sufficient number of vapor molecules in the environment enables the formation of a prominent liquid bridging S-NRs and bacteria, resulting in a significant increase in straining force (as observed in cases with 375 000 to 875 000 water molecules). Additionally, it is worth noting that the enlargement of the condensates size leads to an increase in the radius of curvature r_1, which in turn reduces the corresponding forces F_c (as seen in cases with 50 000 to 875 000 water molecules).[11]

$$F_c = 2\pi\gamma R\sin\Phi\sin(\Phi+\theta) + \frac{\gamma}{r_1}\pi R^2\sin^2\Phi \quad (2)$$

where R is radius of the bacteria sphere; Φ is filling angle; γ is the surface tension of the liquid; θ is the contact angle, shown in Figure S12 (Supporting Information). Notably, the calculated pressure is ≈40 MPa, much higher than the ultimate tensile stress 13 MPa.[19]

Increasing RH will significantly reduce the survival rate to ≈0% on S-NRs at a broad range (≥30%), as shown in Figures 3c and S13 and S14 (Supporting Information), in strong contrast with NRs that kill most bacteria only when RH > 90%. All these results are in good agreement with experimental and theoretical results in previous studies.[45,48]

5. Antibacterial Textiles

We demonstrated potential utilization of S-NRs in personal protective equipment. Similar with glasses, polypropylene (PP) cloth fibers were easily modified with S-NRs, serving as an antibacterial layer in face masks, as shown in **Figures** 4a,b and S15 (Supporting Information). We subsequently assessed the protective efficacy against *E. coli* and *S. aureus*. Following the application of aerosols containing bacteria onto PP fabrics and allowing them to sit for 6 min for *E. coli* and 20 min for *S. aureus* (time period in consistent with tests on S-NRs decorated glass), as depicted in Figures 4c and S16 and S17 (Supporting Information), the cloth decorated with S-NRs showed potent bactericidal activity upon contact. The colony forming units (CFU) decreased to 0. In addition, the PP cloth with S-NRs maintains high antibacterial capacity for up to 6 weeks (Figure 4d; Figure S18, Supporting Information).

Next, we investigated the antimicrobial activities of commercial face mask and commercial mask integrated with S-NRs decorated melt-blown PP cloth. From Figure 4e, in contrast, with the bare commercial mask of incremental bacteria levels residual, it is concluded that the modified mask keeps no measurable levels of living bacteria residual for 5 days. Given that face masks operate in environments both with and without light exposure, we extended our research to test our S-NRs under natural light conditions. The findings, illustrated in Figure S19 (Supporting Information), display comparable antibacterial efficacy to conditions devoid of light. This similarity might arise from the slow-paced formation of reactive oxygen species relative to our antibacterial method, rendering it unable to exert a significant influence. Apart from face mask, S-NRs can be utilized in other fabrics. Consistent with glass slide and PP cloth, S-NRs was successfully introduced on polyethylene terephthalate (PET) and Nylon cloth (Figure 4f; Figures S20 and S21a,b, Supporting Information), indicating that this method has wide adaptability and practicability. As shown in Figures 4g and S21c (Supporting Information), S-NRs modified PET and Nylon cloth provides strong bacteria-killing performances. The above results indicate that manipulated capillary condensation on cloth with S-NRs has huge potential in biological protection against airborne pathogens.

6. Discussion

All these results presented above support our hypothesis that mechanical straining created by fluidic menisci formed during capillary condensation within confined spaces between bacteria and well-designed nanostructures can spontaneously damage and kill microorganisms, for example, *E. coli* and *S. aureus*, as shown in Figure 1a. Experimental studies on ambient humidity-mediated disinfection behaviors of superhydrophilic nanorods, along with the theoretical calculations of corresponding meniscus forces, indicate the feasibility to sterilize bio-aerosols via natural environmental factors, in strong contrast with traditional approaches, such as anti-microbial agents. These findings expand the potential utility of fluid statics for antibacterial strategies into the realm of biofouling-proof biomedical devices or materials. The quick elimination of bacteria, along with the capacity to function over extended periods across various humidity levels, is essential not just for the surgical masks discussed in this article, but also for treating surface wounds on the body, which we plan to address in subsequent work. Further efforts will also seek to graft humidity-responsive polymers, such as polyionic liquid, onto rigid nanorods to enhance the mechano-bactericidal performances.

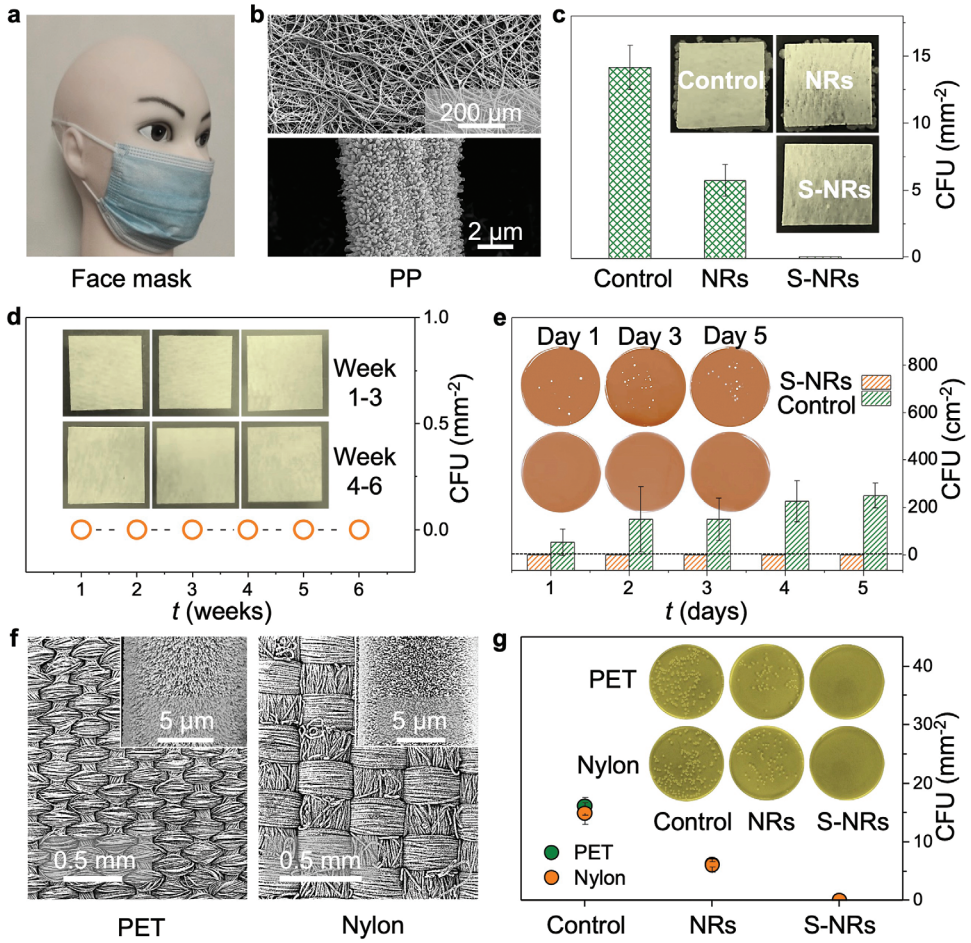

Figure 4. S-NRs-based antibacterial textiles. a,b) Optical photograph and SEM images of S-NRs on PP melt-blown cloth for medical masks. c) CFU of *E. coli* on different PP cloth. Insets represent photographs of corresponding samples (2×2 cm^2). d) Colony formation assay to demonstrate excellent long-term antibacterial performance for up to 6 weeks. No CFU is found as indicated in inset photographs. e) Continuous human wearing (5 days) of untreated medical masks and masks with S-NRs decorated PP cloth as the filter layers, to illustrate the antimicrobial activity. f) SEM images of S-NRs based PET (left) and Nylon (right) cloth. g) The relevant CFU count of *E. coli*, showing different antibacterial performance of control and S-NRs modified cloth. The error bars represent standard deviations and $n = 5$ for each data point.

7. Experimental Section

Materials: Zinc acetate (Sinopharm), Ethanolamine (AR, 99%, Aladdin), 2-Methoxyethanol (AR, Aladdin), Zinc nitrate hexahydrate (98%, Alfa Aesar), Hexamethylenetetramine (99%, International laboratory USA), 3-Methacryloxy propyl trimethoxy silane (KH570, 97%, Alfa Aesar), Benzophenone (BP, 99%, J&K Scientific), N-Vinylpyrrolidone (NVP, 99%, Alfa Aesar), Glutaraldehyde (Alfa Aesar, 50% aq. soln. 50% aq), Phosphate-buffered Saline (PBS, pH 7.4, Sigma), nutrient agar (HKM 02 2021), nutrient broth (HKM 02 2010), SYTO 9 (Thermo Fisher Scientific, 3.34 mM in dimethylsulfoxide), Prodium iodide (PI, Thermo Fisher Scientific, 20 mM in dimethylsulfoxide), Potassium nitrate (KNO_3, AR, DAMAO), Lithium bromide (LiBr, 99%, Aladdin), Potassium acetate (CH_3COOK, 99%, Aladdin), Magnesium chloride ($MgCl_2$, 99%, Aladdin), Potassium carbonate (K_2CO_3, 99%, Aladdin), Magnesium nitrate hexahydrate ($Mg(NO_3)_2 \cdot 6H_2O$, 99%, Sigma–Aldrich), Potassium iodide (KI, 99%, Aladdin), Sodium chloride (NaCl, 99%, Aladdin), Potassium chloride (KCl, 99%, Aladdin), ethanol (AR, UNI-CHEM), deionized water (Thermo Scientific).

Fabrication of NRs and S-NRs on Glass Slide: 1) ZnO seed Solution: Zinc acetate (3.3 g) and 0.915 g of ethanolamine were dissolved in 30 g of glycol methyl ether. The solution underwent ultrasound treatment until no precipitate remained. 2) ZnO growth solution: Zinc nitrate hexahydrate (2.975 g) was dissolved, as well as hexamethylenetetramine (1.4 g) into 1 L distilled water. After ultrarsonic treatment, the growth solution was transparent. 3) NRs Fabrication using the hydrothermal approach: First, the glass slide was sequentially immersed in distilled water and ethanol, sonicated for cleaning purposes for 15 min each. Next, the glass slide was coated with the ZnO seed solution using spin coating (KW-4A, Institute of Microelectronics of the Chinese Academy of Sciences) and incubated it on a hot plate (Heidolph) at 230 °C for 15 min. Lastly, it was immersed in ZnO growth solution, heated for 9 h at 85 °C, and washed with deionized water and dried in air. 4) To prepare S-NRs, the NRs were first put in inductively coupled plasma (ICP) etcher (Trion, Phantom RIE ICP) for 180 s and ≈10 mT oxygen atmospheres. Subsequently, NRs were immersed in solutions of KH570 for 4 h and dried, followed by immersed in solutions of BP for 15 min and dried again. In addition, it was dipped into monomer solutions of NVP and irradiated by a UV light, polymerizing for 1.5 h, and obtaining S-NRs.

Growth of the NRs and S-NRs on Cloth: First, the cloth was immersed in ZnO seed solution for 30 min. Then, it was incubated in on hot plate at 100 °C for 15 min. Next, it was immersed in ZnO growth solution, heated for 12 h at 85 °C, and immersed in deionized water and dried in air. The modification step was same with glass slide and S-NRs-based cloth were obtained.

Characterization of NRs and S-NRs: SEM (Tescan MAIA3) was applied to obtain the morphology of NRs and S-NRs at an accelerating voltage

of 5 kV. EDX was employed to map the element composition on the of NRs and S-NRs. XPS (Thermo Scientific Nexsa) and FT-IR spectra meter (Thermo Scientific Nicolet iS5) were used to obtain the chemical difference between NRs and S-NRs.

Antibacterial Assays: 1) Generation of bacteria-containing aerosol: Gram-positive spherical *S. aureus* (ATCC 6538) and gram-negative rod *E. coli* (CMCC 44 102) were cultured to prepare the corresponding bacteria solution. A single colony of the bacteria on a solid Luria-Bertani agar plate was transferred in 10 mL Luria-Bertani broth for further culture of 24 h at 37 °C. The bacteria solution was washed with PBS and collected with centrifugation (Thermo Fisher Scientific, Centrifuge Pico 17). The bacteria pellet was resuspended with PBS, and the suspension was ready for further experiment. The bacteria concentration was measured by serial dilution and CFU counting. 5 mL of bacteria solution (10^7 CFU mL^{-1}) was added into a compression atomizer (XBK, MCN-S600MF) to generate bio-aerosol. Before this, the water droplets deposited onto glass plate were observed using microscope (Nikon, SMZ1270) to determine the spray distance, as shown in Figure S22 (Supporting Information). 2) The bacteria-containing aerosol (10^7 CFU mL^{-1}) was sprayed onto the sample surface from a distance of 25 cm for 30 s and allowed it to make contact *E. coli* for 6 min and *S. aureus* for 20 min or longer. Subsequently, the bacteria were transferred through ultrasonic rinsing onto agar plates and the plates were incubated at 37 °C for 24 h to assess antibacterial performance. 3) Live/dead fluorescence characterization of bacteria: The green fluorescence SYTO 9 and red fluorescence PI dye were added to the bacterial suspension. After staining for 20 min, the bacteria were washed with PBS and diluted in PBS. The fluorescence was observed and recorded with fluorescence microscopy (Nikon Eclipse Ti2). 4) Humidity control: the antibacterial assays were conducted under a series of humidity via the saturated aqueous solutions method.[49]

SEM Characterization of Bacteria Deposited: Bacteria were harvested from the samples using ultrasonic treatment and washed three times with PBS. The bacterial specimens were fixed in a 2 wt.% glutaraldehyde solution in PBS and were maintained at 4 °C overnight before rinsing them three times with DI water. The bacterial samples were dehydrated through a progressive ethanol/water series, using ethanol concentrations of 30, 50, 70, 90, 95, and 100% for 1 h each. Finally, the bacterial cells were coated with a gold layer to facilitate SEM observations.

Water Contact Angle Measurements of Bacterial Surface: After culturing for 24 h, the *E. coli* cells were collected by centrifugation at 8000×g for 15 min, washed twice with KNO_3 solution (0.1 M), and resuspended. 10 mL bacterial suspension was filtered through a 0.45 µm cellulose acetate filter.[50] A thick layer of cells, density of 10^8 cells per mm^2, was obtained after negative pressure filtration. Then, the wet filter was placed on a glass slide and left it to dry for 90 min. Water contact angle measurement was carried out with sessile drop technique. As shown in Figure S23 (Supporting Information), the water contact angle of *E. coli* cells film was ≈18.1°. This step was to provide parameters to the simulation section.

Simulation Method: Molecular dynamics (MD) simulations were employed to investigate the process of capillary straining formation and to obtain the corresponding force between a S-NR and a bacterium in a humid environment. The simulation comprised four main steps: simplification and construction of the simulation model, determination of potential parameters, formation of liquid bridge, and measurement of liquid bridge force.

Model Simplification and Construction: Figure S24a (Supporting Information) shows the simplified simulation model based on the geometries of the S-NR and bacteria, where a bacterium was placed directly above the S-NR, and the S-NR and bacteria were simplified as a spherocylindrical (i.e., adding a hemisphere at the end of cylinder, diameter ≈ 60 nm) and a cylinder (diameter ≈ 500 nm), respectively. For computation efficiency and without loss of generality, the size of selected simulation domain was set to be ≈80 nm × 80 nm × 40 nm (X × Y × Z) as depicted in Figure S24b,c (Supporting Information). Both the S-NR and bacteria were constructed using face-centered cubic (FCC) crystal with a lattice constant of 0.495 nm, and a thickness of 1.5 nm was set for each structure. Combined with the appropriate potential parameters, such simplification could significantly improve the computation efficiency while maintaining the accuracy of simulation results.

Potential Parameters Determination: To accurately capture the main characteristics of the liquid bridge formation process and obtain precise liquid bridge force, it was crucial to address the wettability of S-NR and bacteria and the properties of water (particularly, surface tension). In this study, the water molecules were simulated by using the classical mW model, a monatomic water model with high computational efficiency and the ability to accurately reproduce the surface tension and other properties of water.[51] Under ambient conditions (101.325 KPa and 300 K), the simulated surface tension via the mW model is ≈66 mN m^{-1}, which is close to the experimental value of ≈72 mN m^{-1}.[52]

The interactions between solid atom and solid atom (S–S) and solid atom and water molecule (S–W) could be described with the well-known 12–6 Lennard-Jones (LJ) potential (see Equation (3)). The wettability of S-NR and bacteria was adjusted by modifying the values of ε_{S-W} and σ_{S-W} in 12–6 LJ potentials.

$$U_{LJ} = 4\varepsilon_{ij}\left[\left(\frac{\sigma_{ij}}{r_{ij}}\right)^{12} - \left(\frac{\sigma_{ij}}{r_{ij}}\right)^{6}\right], r_{ij} \le r_c \quad (3)$$

where ε_{ij} and σ_{ij} represent the potential well depth and collision diameter, respectively, and r_{ij} is the distance between two atoms. The LJ potential is truncated at a cutoff distance r_c = 1 nm.

In accordance with previous works, the value of σ_{S-W} is fixed at 0.3176 nm, while the desired wettability is achieved by adjusting the value of ε_{S-W}.[52] For the simulation model employed in this study, a higher ε_{S-W} value results in a more hydrophilic S-NR /bacteria, with $\cos\theta_E$ (where θ_E denotes the equilibrium contact angle of a water droplet on the S-NR /bacteria surface) increasing linearly with ε_{S-W} (as shown in Figure S25, Supporting Information) under ambient conditions (101.325 KPa and 300 K). An empirical relation between $\cos\theta_E$ and ε_{S-W} was further established in Equation (4).

$$\cos\theta_E = 0.5195\varepsilon_{S-W} - 1.2774 \quad (4)$$

The experimentally measured equilibrium contact angles (θ_E) of water droplets on S-NR and bacteria surfaces were 0° and 18°, respectively. Therefore, the corresponding values of ε_{S-W} were determined to be 0.7849 and 0.7039 kcal mol^{-1}, respectively. With respect to S–S interactions, The values of $\sigma_{S-S} \approx 0.3176$ nm and $\varepsilon_{S-S} \approx 2.5$ kcal mol^{-1} were set, respectively.

Simulation Procedure and Details: To simulate the process of liquid bridge formation in humid environments, water molecules were randomly generated in the simulation domain at a constant rate of one molecule per 500 fs. The total number of water molecules generated reflects the humidity level of the environment, with a larger number of water molecules corresponding to a more humid environment. In this work, eight different humidity levels were considered, corresponding to 0, 125 000, 250 000, 375 000, 500 000, 625 000, 755 000, and 875 000 water molecules generated in the simulation domain. The S-NR and bacteria were fixed to improve computation efficiency, while the water molecules were allowed to move freely in the canonical (NVT) ensemble, and the Nosé-Hoover thermostat was employed to maintain the temperature of water molecules at 300 K.[53] The generation process lasted until the number of water molecules reached the preset value, and an additional simulation time of 50 ns was performed to relax the simulation system to an equilibrium state.

A common strategy to calculate the liquid bridge force between a S-NR and a bacterium was pulling the bacterium away from the S-NR with a constant velocity, during which the liquid bridge force could be obtained. However, the obtained liquid bridge force was sensitive to the moving velocity of the bacterium, seriously undermining the credibility of simulation results.[54] As an alternative, a static method was utilized to measure the liquid bridge bonding force in this work, that is, both the S-NR and bacteria were fixed and remained static during simulations, and the S–S interactions in simulation system were excluded, then the resulting force applied on bacteria was caused by liquid bridge.

The position and velocity of atoms/molecules were updated through the velocity-Verlet algorithm with a time step of 5 fs.[52] Moreover, periodic boundary conditions were adopted in all directions. All MD simulations were performed on the classical platform LAMMPS, and the simulation trajectories were visualized in the open visualization tool OVITO.[55,56]

Supporting Information

Supporting Information is available from the Wiley Online Library or from the author.

Acknowledgements

Y.Z. and H.A. contributed equally to this work. The authors acknowledge the funding of the National Natural Science Foundation of China (no. 21776235, 21376197, and 42377066) and the studentship by the Hong Kong Polytechnic University.

Conflict of Interest

The authors declare no conflict of interest.

Data Availability Statement

The data that support the findings of this study are available from the corresponding author upon reasonable request.

Keywords

antibacterial materials, capillary condensation, liquid bridge, superhydrophilicity, wettability

Received: November 19, 2023
Revised: April 22, 2024
Published online: May 15, 2024

[1] M. Song, Y. Liu, X. Huang, S. Ding, Y. Wang, J. Shen, K. Zhu, *Nat. Microbiol.* **2020**, *5*, 1040.
[2] D. P. Linklater, V. A. Baulin, S. Juodkazis, R. J. Crawford, P. Stoodley, E. P. Ivanova, *Nat. Rev. Microbiol.* **2021**, *19*, 8.
[3] Y. Fan, X.-D. Li, P.-P. He, X.-X. Hu, K. Zhang, J.-Q. Fan, P.-P. Yang, H.-Y. Zheng, W. Tian, Z.-M. Chen, L. Ji, H. Wang, L. Wang, *Sci. Adv.* **2020**, *6*, eaaz4767.
[4] W. Xiu, L. Ren, H. Xiao, Y. Zhang, D. Wang, K. Yang, S. Wang, L. Yuwen, X. Li, H. Dong, Q. Li, Y. Mou, Y. Zhang, Z. Yin, B. Liang, Y. Gao, L. Wang, *Sci. Adv.* **2023**, *9*, eade5446.
[5] H. Zhang, Q. Chen, J. Xie, Z. Cong, C. Cao, W. Zhang, D. Zhang, S. Chen, J. Gu, S. Deng, Z. Qiao, X. Zhang, M. Li, Z. Lu, R. Liu, *Sci. Adv.* **2023**, *9*, eabn0771.
[6] Q. Yang, P. Z. Sun, L. Fumagalli, Y. V. Stebunov, S. J. Haigh, Z. W. Zhou, I. V. Grigorieva, F. C. Wang, A. K. Geim, *Nature* **2020**, *588*, 250.
[7] L. R. Fisher, R. A. Gamble, J. Middlehurst, *Nature* **1981**, *290*, 575.
[8] W. Hirst, *Nature* **1947**, *159*, 267.
[9] R. C. Major, J. E. Houston, M. J. McGrath, J. I. Siepmann, X.-Y. Zhu, *Phys. Rev. Lett.* **2006**, *96*, 177803.
[10] S. J. Park, C. H. Lee, Y. Kim, J. H. Ko, T. Kim, S. J. Kim, S. Nahm, H. Cho, M.-W. Moon, *Proc. Natl. Acad. Sci. U. S. A.* **2022**, *119*, 2209586119.
[11] X. Xiao, L. Qian, *Langmuir* **2000**, *16*, 8153.
[12] J. W. van Honschoten, N. R. Tas, M. Elwenspoek, *Am. J. Phys.* **2010**, *78*, 277.
[13] W. Xin, J. Fu, Y. Qian, L. Fu, X.-Y. Kong, T. Ben, L. Jiang, L. Wen, *Nat. Commun.* **2022**, *13*, 1701.
[14] S. Li, B. Deng, A. Grinthal, A. Schneider-Yamamura, J. Kang, R. S. Martens, C. T. Zhang, J. Li, S. Yu, K. Bertoldi, J. Aizenberg, *Nature* **2021**, *592*, 386.
[15] M. Prakash, D. Quere, J. W. Bush, *Science* **2008**, *320*, 931.
[16] J. Tang, Y. Zhao, M. Wang, D. Wang, X. Yang, R. Hao, M. Wang, Y. Wang, H. He, J. H. Xin, S. Zheng, *Nat. Commun.* **2022**, *13*, 1291.
[17] G. Xie, P. Li, P. Y. Kim, P.-Y. Gu, B. A. Helms, P. D. Ashby, L. Jiang, T. P. Russell, *Nat. Chem.* **2022**, *14*, 208.
[18] Y. Zhao, J. Wang, X.-Y. Kong, W. Xin, T. Zhou, Y. Qian, L. Yang, J. Pang, L. Jiang, L. Wen, *Natl. Sci. Rev.* **2020**, *7*, 1349.
[19] H. A., Z. Yang, R. Hu, Y. F. Chen, *Langmuir* **2023**, *39*, 2932.
[20] J. Q. Yang, J. E. Sanfilippo, N. Abbasi, Z. Gitai, B. L. Bassler, H. A. Stone, *Proc. Natl. Acad. Sci. U. S. A.* **2021**, *118*, 2111060118.
[21] E. P. Ivanova, D. P. Linklater, M. Werner, V. A. Baulin, X. Xu, N. Vrancken, S. Rubanov, E. Hanssen, J. Wandiyanto, V. K. Truong, A. Elbourne, S. Maclaughlin, S. Juodkazis, R. J. Crawford, *Proc. Natl. Acad. Sci. U. S. A.* **2020**, *117*, 12598.
[22] B. Peng, X. Zhang, D. Aarts, R. P. A. Dullens, *Nat. Nanotechnol.* **2018**, *13*, 478.
[23] A. del Valle, J. Torra, P. Bondia, C. M. Tone, P. Pedraz, V. Vadillo-Rodriguez, C. Flors, *ACS Appl. Mater. Interfaces* **2020**, *12*, 31235.
[24] J. Jenkins, J. Mantell, C. Neal, A. Gholinia, P. Verkade, A. H. Nobbs, B. Su, *Nat. Commun.* **2020**, *11*, 1626.
[25] A. Martínez-Calvo, T. Bhattacharjee, R. K. Bay, H. N. Luu, A. M. Hancock, N. S. Wingreen, S. S. Datta, *Proc. Natl. Acad. Sci. U. S. A.* **2022**, *119*, 2208019119.
[26] S. Luan, J. Zhao, H. Yang, H. Shi, J. Jin, X. Li, J. Liu, J. Wang, J. Yin, P. Stagnaro, *Colloids Surf., B* **2012**, *93*, 127.
[27] X. Liu, Y. Xu, Z. Wu, H. Chen, *Macromol. Biosci.* **2103**, *13*, 147.
[28] X. Feng, L. Feng, M. Jin, J. Zhai, L. Jiang, D. Zhu, *J. Am. Chem. Soc.* **2004**, *126*, 62.
[29] T. Bhattacharjee, S. S. Datta, *Nat. Commun.* **2019**, *10*, 2075.
[30] C. J. Landry, F. P. Burns, F. Baerlocher, K. Ghandi, *Adv. Funct. Mater.* **2018**, *28*, 1706309.
[31] J. Zhou, N. S. Xu, Z. L. Wang, *Adv. Mater.* **2006**, *18*, 2432.
[32] B. Ortiz-Casas, A. Galdámez-Martínez, J. Gutiérrez-Flores, A. B. Ibañez, P. K. Panda, G. Santana, H. Astudillo de la Vega, M. Suar, C. G. Rodelo, A. Kaushik, Y. K. Mishra, A. Dutt, *Mater. Today* **2021**, *50*, 533.
[33] S. V. Gudkov, D. E. Burmistrov, D. A. Serov, M. B. Rebezov, A. A. Semenova, A. B. Lisitsyn, *Front. Phys.* **2021**, *9*, 641481.
[34] J. Joo, B. Y. Chow, M. Prakash, E. S. Boyden, J. M. Jacobson, *Nat. Mater.* **2011**, *10*, 596.
[35] I. Lee, J. Kim, R. Kwak, J. Lee, *Adv. Funct. Mater.* **2023**, *33*, 2213650.
[36] N. N. Song, Y. Yu, Y. Zhang, Z. Wang, Z. Guo, J. Zhang, C. Zhang, M. Liang, *Adv. Mater.* **2024**, *36*, 2210455.
[37] A. Elbourne, R. J. Crawford, E. P. Ivanova, *J. Colloid Interface Sci.* **2017**, *508*, 603.
[38] S. Zhao, Z. Li, D. P. Linklater, L. Han, P. Jin, L. Wen, C. Chen, D. Xing, N. Ren, K. Sun, S. Juodkazis, E. P. Ivanova, L. Jiang, *Nano Lett.* **2022**, *22*, 1129.
[39] H. Zhu, F. Xia, *Matter* **2022**, *5*, 785.
[40] Y. Zhang, J. Cui, K.-Y. Chen, S. H. Kuo, J. Sharma, R. Bhatta, Z. Liu, A. Ellis-Mohr, F. An, J. Li, Q. Chen, K. D. Foss, H. Wang, Y. Li, A. M. McCoy, G. W. Lau, Q. Cao, *Sci. Adv.* **2023**, *9*, eadg7397.
[41] B. Clarke, K. Ghandi, *Small* **2023**, *19*, 2302864.
[42] G. Milano, L. D'Ortenzi, K. Bejtka, L. Mandrile, A. M. Giovannozzi, L. Boarino, C. F. Pirri, C. Ricciardi, S. Porro, *J. Phys. Chem. C* **2018**, *122*, 8011.

[43] T.-N. Le, A.-N. Au-Duong, C.-K. Lee, *J. Membr. Sci.* **2019**, *574*, 164.
[44] A.-N. Au-Duong, C.-K. Lee, *Colloid Polym. Sci.* **2018**, *296*, 1173.
[45] C. Birleanu, M. Pustan, F. Rusu, C. Dudescu, R. Muller, A. Baracu, *Microsyst. Technol.* **2018**, *28*, 1.
[46] A. Çolak, H. Wormeester, H. J. W. Zandvliet, B. Poelsema, *Appl. Surf. Sci.* **2012**, *258*, 6938.
[47] S. Peng, B. Xie, Y. Wang, M. Wang, X. Chen, X. Ji, C. Zhao, G. Lu, D. Wang, R. Hao, M. Wang, N. Hu, H. He, Y. Ding, S. Zheng, *Proc. Natl. Acad. Sci. U. S. A.* **2023**, *120*, 2303466120.
[48] A. Fukunishi, Y. Mori, *Adv. Powder Technol.* **2006**, *17*, 567.
[49] L. Greenspan, *J. Res. Natl. Bur. Stand. A. Phys. Chem.* **1977**, *81A*, 89.
[50] H. J. Busscher, A. H. Weerkamp, H. C. van der Mei, A. W. van Pelt, H. P. de Jong, J. Arends, *Appl. Environ. Microbiol.* **1984**, *48*, 980.
[51] V. Molinero, E. B. Moore, *J. Phys. Chem. B* **2009**, *113*, 4008.
[52] H. A., Z. Yang, R. Hu, Y. F. Chen, *J. Colloid Interface Sci.* **2022**, *607*, 1023.
[53] H. A., Z. Yang, R. Hu, Y.-F. Chen, L. Yang, *J. Phys. Chem. C* **2020**, *124*, 23260.
[54] S. Cheng, M. O. Robbins, *Phys. Rev. E: Stat., Nonlinear, Soft Matter Phys.* **2014**, *89*, 062402.
[55] A. P. Thompson, H. M. Aktulga, R. Berger, D. S. Bolintineanu, W. M. Brown, P. S. Crozier, P. J. in 't Veld, A. Kohlmeyer, S. G. Moore, T. D. Nguyen, R. Shan, M. J. Stevens, J. Tranchida, C. Trott, S. J. Plimpton, *Comput. Phys. Commun.* **2022**, *271*, 108171.
[56] A. Stukowski, *Modell. Simul. Mater. Sci. Eng.* **2010**, *18*, 015012.